

The Elastic–Viscous–Plastic Sea Ice Dynamics Model in General Orthogonal Curvilinear Coordinates on a Sphere—Incorporation of Metric Terms

ELIZABETH C. HUNKE AND JOHN K. DUKOWICZ

Group T-3, Los Alamos National Laboratory, Los Alamos, New Mexico

(Manuscript received 16 July 2001, in final form 10 December 2001)

ABSTRACT

A new discretization for the elastic–viscous–plastic (EVP) sea ice dynamics model incorporates metric terms to account for grid curvature effects in curvilinear coordinate systems. A fundamental property of the viscous–plastic ice rheology that is invariant under changes of coordinate system is utilized; namely, the work done by internal forces, to derive an energy dissipative discretization of the divergence of the stress tensor that includes metric terms. Comparisons of simulations using an older EVP numerical model with the new formulation highlight the effect of the metric terms, which can be significant when ice deformation is allowed to affect the ice strength.

1. Introduction

Sea ice dynamics models (Hibler 1979; Flato and Hibler 1992; Hunke and Dukowicz 1997, for example) are typically formulated and applied in Cartesian coordinates for simplicity, and therefore neglect metric terms (terms due to grid curvature). In reality, however, these models exist on a spherical manifold and are preferably applied in curvilinear coordinates, where metric terms exist and may be important. Recently general orthogonal grids in which pole singularities are moved smoothly into nearby land masses have gained in popularity for use in global climate simulations. On such grids converging meridians at the poles are not a serious problem for ocean and sea ice models because the pole is outside the solution domain. However, metric terms can be large because of the rapidly varying grid in the vicinity of the poles, and model discretizations should take them into account. The inclusion of metric terms is a nontrivial algebraic exercise; the objective of this paper is to incorporate metric terms in the elastic–viscous–plastic (EVP) model (Hunke and Dukowicz 1997).

Metric terms arise in two ways in a sea ice dynamics model. They arise in the formulation of the strain rate and in the representation of the stress divergence. The EVP model from the outset derived the stress divergence by a variational method based on the internal work of the sea ice rheology. Since the internal work is a scalar quantity, independent of the manifold or coordinate system used, the stress divergence forces so derived automatically include metric terms. An important addi-

tional benefit of this method when used to obtain a discretization is that it inherently preserves the dissipative nature of the viscous–plastic ice rheology. Thus, the only source of metric term error in the EVP model is the approximation used in specifying the strain rate.

In this paper we remove this source of error by specifically including metric terms in the representation of the strain rate. In general we follow the methodology introduced in Dukowicz and Baumgardner (2002) by making use of a bilinear representation of velocity and stress in each grid cell. This improves the accuracy of the discretization and eliminates the possibility of computational modes.

While the formulation presented later holds for general orthogonal, curvilinear coordinates on a sphere, we present simulation results and comparisons for two specific displaced pole grids, shown in Fig. 1. The 100×116 “Gx3” mesh shown in Fig. 1a covers the globe from 78°S to 90°N . The Southern Hemisphere grid is a regular latitude–longitude mesh, with its equator lying atop the physical equator and the South Pole at 90°S . The grid’s northern pole lies in Greenland, and the mesh size at mid and high latitudes is approximately 3° , with the latitudinal resolution higher near the equator. The grid shown in Fig. 1b, termed the Gx1 grid, is geometrically identical to the Gx3 grid, but with 320×384 nodes, it features approximately 1° resolution. Details regarding displaced pole grids such as these can be found in Smith et al. (1995).

Although the simulations described later were performed on these global grids, we will focus only on results in the Northern Hemisphere. Southern Hemisphere results are less striking because the mesh is more uniform, with land boundaries extending further from the pole.

Corresponding author address: Dr. Elizabeth C. Hunke, MS-B216, Los Alamos National Laboratory, Los Alamos, NM 87545.
E-mail: eclare@lanl.gov

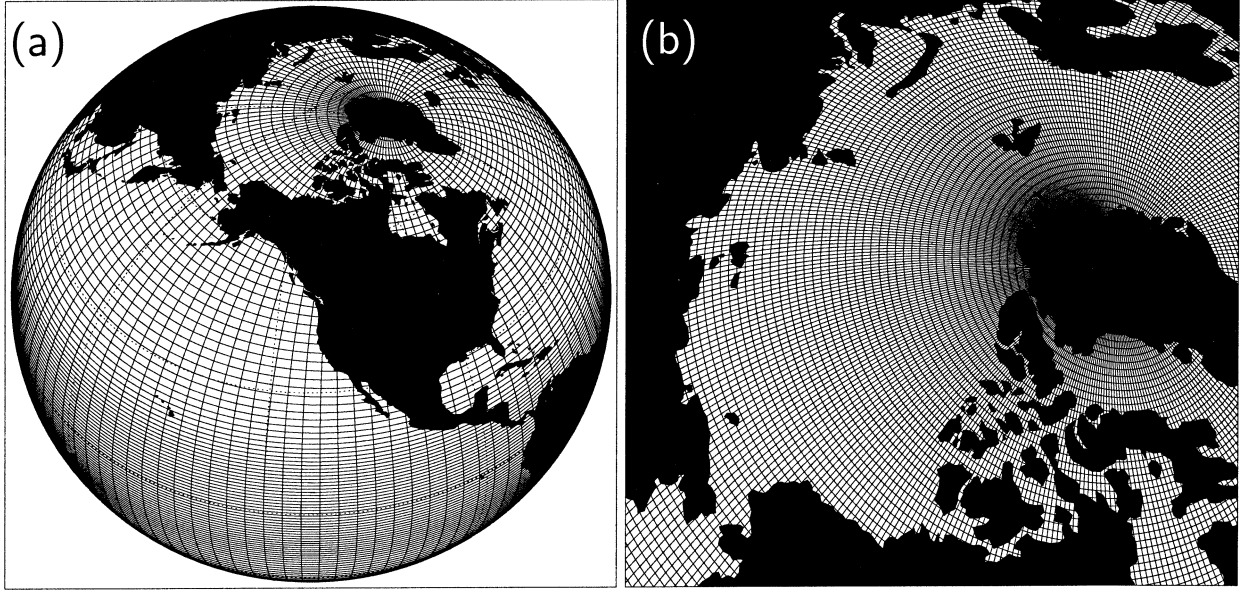


FIG. 1. (a) 100×116 Gx3 global grid, (b) 320×384 Gx1 global grid, for which only the Arctic is shown.

2. Mathematical formulations

a. General framework

We begin by describing the EVP model equations and the variational method in a form independent of a coordinate system, before considering them in curvilinear coordinates. Following Dukowicz and Baumgardner (2002), we introduce the divergence, D_D , and the horizontal tension and shearing strain rates, D_T and D_S , respectively, as

$$D_D = \dot{\epsilon}_{11} + \dot{\epsilon}_{22} \quad D_T = \dot{\epsilon}_{11} - \dot{\epsilon}_{22} \quad D_S = 2\dot{\epsilon}_{12},$$

where $\dot{\epsilon}_{11}$, $\dot{\epsilon}_{22}$, and $\dot{\epsilon}_{12}$ are the components of a symmetric strain rate tensor.

In the viscous-plastic (VP; Hibler 1979) and EVP models, an elliptical yield curve characterizes the ice rheology. Letting $\sigma_1 = \sigma_{11} + \sigma_{22}$ and $\sigma_2 = \sigma_{11} - \sigma_{22}$, where σ_{ij} represents the internal stress tensor of the ice, the EVP model incorporates the constitutive law in the time-dependent equations

$$\frac{1}{E} \frac{\partial \sigma_1}{\partial t} + \frac{\sigma_1}{2\zeta} + \frac{P}{2\zeta} = D_D, \quad (1)$$

$$\frac{1}{E} \frac{\partial \sigma_2}{\partial t} + \frac{\sigma_2}{2\eta} = D_T, \quad (2)$$

$$\frac{1}{E} \frac{\partial \sigma_{12}}{\partial t} + \frac{\sigma_{12}}{2\eta} = \frac{1}{2} D_S, \quad (3)$$

where the symbols are defined in appendix A. Here,

$$\zeta = \frac{P}{2\Delta}, \quad \eta = \frac{P}{2e^2\Delta}, \quad (4)$$

$$\Delta = \left[D_D^2 + \frac{1}{e^2} (D_T^2 + D_S^2) \right]^{1/2}, \quad (5)$$

and P is the ice strength that depends on the particular parameterization used. The VP model is recovered at steady state:

$$\sigma_1 = 2\zeta D_D - P, \quad (6)$$

$$\sigma_2 = 2\eta D_T, \quad (7)$$

$$\sigma_{12} = \eta D_S. \quad (8)$$

Equations (1)–(3) as well as (6)–(8) describe a nonlinear constitutive law that relates the internal stress tensor to the rates of strain. Note that the constitutive law presumes that $\Delta \neq 0$. When the ice is rigid and rates of strain are zero, $\Delta = 0$ and the viscosities η and ζ would be infinite; in that case the VP and EVP models must both employ a regularization method. The VP model simply limits the viscosities (Hibler 1979), while the EVP model makes use of elastic waves to regularize the singularity (Hunke and Dukowicz 1997; Hunke 2001).

Both EVP and VP models utilize the vertically integrated momentum equations

$$m \frac{\partial u}{\partial t} = F_1 + \tau_1, \quad (9)$$

$$m \frac{\partial v}{\partial t} = F_2 + \tau_2. \quad (10)$$

Equations (9) and (10) determine the ice velocity based on the internal ice forces, F_1 and F_2 , and the surface forcing, τ_1 and τ_2 . Surface forcing terms include wind stress, ocean stress, tilt of the ocean surface and a Coriolis term, as described in Hibler (1979) and Hunke and Dukowicz (1997). The two components of the internal stress force, F_1 and F_2 , are given in Cartesian coordinates as the stress divergence:

$$F_1 = \frac{\partial \sigma_{11}}{\partial x} + \frac{\partial \sigma_{12}}{\partial y}, \quad (11)$$

$$F_2 = \frac{\partial \sigma_{12}}{\partial x} + \frac{\partial \sigma_{22}}{\partial y}. \quad (12)$$

These expressions are much more complex in general orthogonal curvilinear coordinates. Our main objective in this paper is to derive a consistent discretization of these forces that fully incorporates all metric terms.

Given the rates of strain $\dot{\epsilon}_{ij}$ and the internal stresses σ_{ij} , the total rate of internal work over an area A is given by the negative of

$$D = \int (\sigma_{11}\dot{\epsilon}_{11} + 2\sigma_{12}\dot{\epsilon}_{12} + \sigma_{22}\dot{\epsilon}_{22}) dA.$$

At steady state (or for the VP model), the stresses are given by a constitutive law, Eqs. (4)–(8), and

$$\begin{aligned} D &= \int \left[\frac{1}{2}\sigma_1 D_D + \frac{1}{2}\sigma_2 D_T + \sigma_{12} D_S \right] dA \\ &= \frac{1}{2} \int P(\Delta - D_D) dA \geq 0. \end{aligned} \quad (13)$$

In this case, D is the positive definite dissipation rate, indicating that the system dissipates energy. Note that for the EVP model, D is not just the dissipation rate but also contains a contribution from stored elastic energy.

This dissipation of energy is a fundamental property of the visco-plastic rheology. It is important to preserve this property in the discretization such that the discrete system dissipates energy in the same manner as the continuous system.

b. Transformation to curvilinear coordinates

Assume that u and v represent velocity components in an orthogonal, curvilinear coordinate system along nondimensional coordinates ξ_1 and ξ_2 with scale factors h_1 and h_2 , respectively. Using formulas provided in Batchelor (1967), we find

$$D_S = 2\dot{\epsilon}_{12} = \frac{h_1}{h_2} \frac{\partial}{\partial \xi_2} \left(\frac{u}{h_1} \right) + \frac{h_2}{h_1} \frac{\partial}{\partial \xi_1} \left(\frac{v}{h_2} \right), \quad (14)$$

$$D_T = \dot{\epsilon}_{11} - \dot{\epsilon}_{22} = \frac{h_2}{h_1} \frac{\partial}{\partial \xi_1} \left(\frac{u}{h_2} \right) - \frac{h_1}{h_2} \frac{\partial}{\partial \xi_2} \left(\frac{v}{h_1} \right), \quad (15)$$

$$D_D = \dot{\epsilon}_{11} + \dot{\epsilon}_{22} = \frac{1}{h_1 h_2} \left[\frac{\partial}{\partial \xi_1} (h_2 u) + \frac{\partial}{\partial \xi_2} (h_1 v) \right]. \quad (16)$$

These expressions for the strain rates incorporate metric terms since they contain derivatives of the scale factors.

The strain rates may be written out as follows,

$$D_S = \left[\frac{1}{h_2} \frac{\partial u}{\partial \xi_2} + \frac{1}{h_1} \frac{\partial v}{\partial \xi_1} \right] - \left[\frac{1}{h_1 h_2} \frac{\partial h_1}{\partial \xi_2} u + \frac{1}{h_1 h_2} \frac{\partial h_2}{\partial \xi_1} v \right], \quad (17)$$

$$D_T = \left[\frac{1}{h_1} \frac{\partial u}{\partial \xi_1} - \frac{1}{h_2} \frac{\partial v}{\partial \xi_2} \right] - \left[\frac{1}{h_1 h_2} \frac{\partial h_2}{\partial \xi_1} u - \frac{1}{h_1 h_2} \frac{\partial h_1}{\partial \xi_2} v \right], \quad (18)$$

$$D_D = \left[\frac{1}{h_1} \frac{\partial u}{\partial \xi_1} + \frac{1}{h_2} \frac{\partial v}{\partial \xi_2} \right] + \left[\frac{1}{h_1 h_2} \frac{\partial h_2}{\partial \xi_1} u + \frac{1}{h_1 h_2} \frac{\partial h_1}{\partial \xi_2} v \right]. \quad (19)$$

Observe that the first pair of terms on the right-hand side is unchanged for a Cartesian grid (constant h_i), while the second pair vanishes. The second pair of terms therefore represents the metric terms. Observe also that the first pair of terms vanishes for a uniform velocity field, while the metric terms do not. Since the strain rates in the original EVP model vanish for a uniform velocity field, we conclude that the EVP model did not contain metric terms. However, the magnitude of the ratio of the metric terms and the Cartesian strain rates varies inversely with the ratio of the spatial scales of variation for the scale factors h_i and the velocity. Since normally the velocity varies on much shorter scales than the grid, it is usually a good assumption to neglect the metric terms, as in the original EVP model. This may not be true in the vicinity of grid singularities, however, as mentioned earlier.

As a concrete example, consider the case of spherical coordinates, obtained through the substitution $\xi_1 = \theta$ (longitude), $\xi_2 = \phi$ (latitude), $h_1 = r \cos \phi$, $h_2 = r$, assuming that there is no gradient nor any motion in the vertical (r) direction. For this case the equations become

$$D_S = \frac{1}{r \cos \phi} \frac{\partial v}{\partial \theta} + \frac{1}{r} \frac{\partial u}{\partial \phi} + \frac{u}{r} \tan \phi,$$

$$D_T = \frac{1}{r \cos \phi} \frac{\partial u}{\partial \theta} - \frac{1}{r} \frac{\partial v}{\partial \phi} - \frac{v}{r} \tan \phi,$$

$$D_D = \frac{1}{r \cos \phi} \frac{\partial u}{\partial \theta} + \frac{1}{r} \frac{\partial v}{\partial \phi} - \frac{v}{r} \tan \phi,$$

and the metric terms are $u \tan \phi / r$ and $v \tan \phi / r$.

The standard approach to deriving the stress divergence in general orthogonal coordinates is by tensor analysis, which is complex and intimidating. Nevertheless, the appropriate results for the quasi-two-dimensional case of interest here may be found in Aris (1962), for example, and the stress force components may be expressed as follows:

$$F_1 = \frac{1}{2} \left[\frac{1}{h_1} \frac{\partial \sigma_1}{\partial \xi_1} + \frac{1}{h_1 h_2^2} \frac{\partial}{\partial \xi_1} (h_2^2 \sigma_2) + \frac{2}{h_1^2 h_2} \frac{\partial}{\partial \xi_2} (h_1^2 \sigma_{12}) \right], \quad (20)$$

$$F_2 = \frac{1}{2} \left[\frac{1}{h_2} \frac{\partial \sigma_1}{\partial \xi_2} - \frac{1}{h_1^2 h_2} \frac{\partial}{\partial \xi_2} (h_1^2 \sigma_2) + \frac{2}{h_1 h_2^2} \frac{\partial}{\partial \xi_1} (h_2^2 \sigma_{12}) \right]. \quad (21)$$

These expressions correspond to the Cartesian forms (11) and (12) but now they contain metric terms since they involve derivatives of the scale factors. These are rather complicated expressions. Attempts to discretize them generally fail to guarantee that the discretization is dissipative; that is, that it is consistent with the discrete version of (13). However, we can guarantee this, and also the absence of computational modes, by following the variational methodology of Hunke and Dukowicz (1997) and Dukowicz and Baumgardner (2002).

We observe that the total dissipation rate D is a scalar quantity that is unchanged in any coordinate system. Therefore, by manipulating D we will be able to extract the correct force components in any coordinate system, including the appropriate metric terms. We will illustrate the procedure in the continuous case first, to use later as a guide for our derivation of the discretization.

Integrating the dissipation rate by parts,

$$D = \int \left\{ \frac{1}{2} \sigma_1 \left[\frac{1}{h_1 h_2} \left(\frac{\partial}{\partial \xi_1} (h_2 u) + \frac{\partial}{\partial \xi_2} (h_1 v) \right) \right] + \frac{1}{2} \sigma_2 \left[\frac{h_2}{h_1} \frac{\partial}{\partial \xi_1} \left(\frac{u}{h_2} \right) - \frac{h_1}{h_2} \frac{\partial}{\partial \xi_2} \left(\frac{v}{h_1} \right) \right] + \sigma_{12} \left[\frac{h_1}{h_2} \frac{\partial}{\partial \xi_2} \left(\frac{u}{h_1} \right) + \frac{h_2}{h_1} \frac{\partial}{\partial \xi_1} \left(\frac{v}{h_2} \right) \right] \right\} h_1 h_2 d\xi_1 d\xi_2 \quad (22)$$

$$\begin{aligned} &= -\frac{1}{2} \int \left\{ u \left[\frac{1}{h_1} \frac{\partial \sigma_1}{\partial \xi_1} + \frac{1}{h_1 h_2^2} \frac{\partial}{\partial \xi_1} (h_2^2 \sigma_2) + \frac{2}{h_1^2 h_2} \frac{\partial}{\partial \xi_2} (h_1^2 \sigma_{12}) \right] + v \left[\frac{1}{h_2} \frac{\partial \sigma_1}{\partial \xi_2} - \frac{1}{h_1^2 h_2} \frac{\partial}{\partial \xi_2} (h_1^2 \sigma_2) + \frac{2}{h_1 h_2^2} \frac{\partial}{\partial \xi_1} (h_2^2 \sigma_{12}) \right] \right\} h_1 h_2 d\xi_1 d\xi_2 \\ &\quad + \oint u \left[\frac{1}{2} h_2 (\sigma_1 + \sigma_2) + h_1 \sigma_{12} \right] + v \left[\frac{1}{2} h_1 (\sigma_1 - \sigma_2) + h_2 \sigma_{12} \right] dS \\ &= - \int (u F_1 + v F_2) dA + \text{boundary terms}, \end{aligned} \quad (23)$$

where F_1 and F_2 are the components of the stress divergence as given by (20) and (21), respectively. This, therefore, is an alternative method of obtaining the stress force components, which now are explicitly related to the dissipation rate.

Note that if the domain is surrounded by land or if the ice pack is completely contained within the domain, so that $\mathbf{u} = 0$ on the boundaries, then the boundary terms are zero. However, if the boundary is open or if periodic boundary conditions are used, as on a global, topologically cylindrical grid, then these boundary conditions can be nonzero and they must be accounted for. The discretization method described later accounts for them implicitly.

Equation 23 suggests the following variational computation to obtain stress force components from the dissipation:

$$F_1 = -\frac{1}{dA} \frac{\delta D}{\delta u}, \quad F_2 = -\frac{1}{dA} \frac{\delta D}{\delta v},$$

where the variation is performed assuming that the stress components are not functions of velocity. This may now be used directly to obtain a discretization, given a discrete expression for D . Note that we only need a correct curvilinear expression for the integrand of (13), that is, $(1/2)\sigma_1 D_D + (1/2)\sigma_2 D_T + \sigma_{12} D_S$, including, in particular, the metric terms appearing in the strain rates D_D , D_T , and D_S .

3. Discrete formulations

A discrete formulation is derived by expanding the velocity and stress components in (22) in terms of basis functions. For example, the u component of velocity in grid cell k may be expressed as

$$u_k(\xi_1, \xi_2) = \sum_i u_{ik} \psi_{ik}(\xi_1, \xi_2) \quad (24)$$

where u_{ik} is the discrete velocity associated with vertex i , and ψ_{ik} are the associated basis functions, and similarly for the stress components. Substituting (24) into (22) from all cells k , integrating, and collecting all terms associated with vertex velocities, we obtain the vertex forces corresponding to (20) and (21), as described in more detail later.

Previous discretizations of the EVP model used linear basis functions for the velocities (Hunke and Dukowicz 1997; Hunke 2001). The original discretization method employed four subtriangles within each grid cell, with each triangle having one leg along a cell edge and the four triangles meeting in the center of the cell (see Fig. 1 in Hunke and Dukowicz 1997). The internal ice stress was assumed constant within each triangle, and the strain rates were computed using lengths associated with that triangle. Thus, there were four different values for the strain rates and the internal stress within each grid cell, effectively mitigating the “checkerboard” solution on the B-grid. In this manner, the nonuniformity of the

grid was partially incorporated into the discretization, but, since the strain rates vanish for a constant velocity field, the metric terms associated with the strain rates were not included.

Although the original formulation performed well when compared with the VP model in realistic simulations (Hunke and Zhang 1999), the ice internal stress exhibited undesirable behavior by not converging to the elliptical yield surface on which it is defined. A new numerical formulation to address this issue altered the original discretization to maintain efficiency while obtaining a more accurate solution of the nonlinear equations (Hunke 2001). In the second formulation, four triangles—each containing constant strain rates and internal stress—again tile the grid cell, but this time each triangle covers half the cell and they overlap one another in pairs: (a) northeast–southwest and (b) northwest–southeast. In order for the strain rate and stress values to be consistent, sums over the triangles in case a must equal sums over the case b triangles, and this is only possible if the grid cell center lengths are used when discretizing derivatives. Thus, while this discretization still incorporates varying grid cell sizes over the mesh, it does not include varying grid lengths over each cell as did the original formulation. Metric terms again were not included.

The second formulation features other desirable properties, including a new definition of the elastic parameter E that allows elastic waves to damp out more quickly and ensures that the internal stresses converge to the elliptical yield surface appropriately (Hunke 2001). The changes described here still incorporate these features, and for this reason we will focus the comparison studies described later on the second formulation instead of the original. We will refer to the second formulation as the Cartesian discretization because the strain rates do not contain metric terms.

The present formulation, hereafter referred to as the curvilinear discretization, uses approximations for the velocity and the internal stress that vary bilinearly over each grid cell. That is, for the velocity components,

$$\begin{aligned} u(\xi_1, \xi_2) &= u^{ne}\xi_1\xi_2 + u^{nw}(1 - \xi_1)\xi_2 \\ &\quad + u^{sw}(1 - \xi_1)(1 - \xi_2) + u^{se}\xi_1(1 - \xi_2), \\ v(\xi_1, \xi_2) &= v^{ne}\xi_1\xi_2 + v^{nw}(1 - \xi_1)\xi_2 \\ &\quad + v^{sw}(1 - \xi_1)(1 - \xi_2) + v^{se}\xi_1(1 - \xi_2), \end{aligned}$$

where $\xi_1, \xi_2 \in [0, 1]$. Similar relations hold for the internal ice stress tensor, with one important difference. Because this model is discretized for a B-grid, on which the velocity components for cell (i, j) reside at the northeast corner, we must have $u_{ij}^{ne} = u_{i+1,j}^{nw}$, for example (i, j now represent grid indices); that is, velocity is continuous across cell edges. The internal ice stress, on the other hand, is associated with velocity gradients (through strain rates) that are discontinuous across cell edges, and therefore we maintain four corner values for stress in each cell throughout the integration.

tinuous across cell edges, and therefore we maintain four corner values for stress in each cell throughout the integration.

This may seem peculiar in view of the well-known condition requiring continuity of stress across boundaries. Such a condition is required to prevent infinite accelerations at a boundary. However, as this is a discrete model, the momentum equation is only satisfied in a mean sense over a finite volume and not at a cell boundary. Furthermore, in this model there are no internal material discontinuities since ice boundaries are determined by the ice concentration, which varies continuously. The situation is similar in the previous discretizations of the EVP model in that there is no requirement for the continuity of stress across cell boundaries.

All three of the discretizations are formally second-order accurate. The new discretization method, in which stresses and strain rates are bilinear across each grid cell, contains a more complete representation of velocity and stress, and therefore should be more accurate. Dukowicz and Baumgardner (2002) show that the analogous operator in their case is more isotropic although of the same formal order of accuracy. As was true for the previous discretizations, the checkerboard solution is not a problem in the new formulation; technically, the model is not discretized on a B-grid because we do not have a single value for the internal stress residing at the center of each grid cell.

a. Strain rates

Assume that \mathbf{u} is bilinear in a unit grid cell. Also, because the grids we use are continuously differentiable and relatively smooth, it is a good assumption that $h_1 = \bar{h}_1$, $h_2 = \bar{h}_2$, the midcell grid lengths formed by averaging the two outside edge lengths, and that $\partial h_1 / \partial \xi_2 = \Delta_2 h_1$, $\partial h_2 / \partial \xi_1 = \Delta_1 h_2$, which are simple differences in the grid edge lengths. Then

$$\begin{aligned} &\frac{h_2}{h_1} \frac{\partial}{\partial \xi_1} \left(\frac{u}{h_2} \right) \\ &= \frac{1}{h_1 h_2} \left(h_2 \frac{\partial u}{\partial \xi_1} - u \frac{\partial h_2}{\partial \xi_1} \right) \\ &\approx \frac{1}{h_1 \bar{h}_2} \{ \bar{h}_2 [u^{ne}\xi_2 - u^{nw}\xi_2 - u^{sw}(1 - \xi_2) + u^{se}(1 - \xi_2)] \\ &\quad - \Delta_1 h_2 [u^{ne}\xi_1\xi_2 + u^{nw}(1 - \xi_1)\xi_2 \\ &\quad + u^{sw}(1 - \xi_1)(1 - \xi_2) \\ &\quad + u^{se}\xi_1(1 - \xi_2)] \}. \end{aligned}$$

Similarly,

$$\begin{aligned} \frac{h_1}{h_2} \frac{\partial}{\partial \xi_2} \left(\frac{v}{h_1} \right) \\ \approx \frac{1}{\bar{h}_1 \bar{h}_2} \{ \bar{h}_1 [v^{ne} \xi_2 - v^{nw} \xi_2 - v^{sw} (1 - \xi_2) + v^{se} (1 - \xi_2)] \\ - \Delta_2 h_1 [v^{ne} \xi_1 \xi_2 + v^{nw} (1 - \xi_1) \xi_2 \\ + v^{sw} (1 - \xi_1) (1 - \xi_2) \\ + v^{se} \xi_1 (1 - \xi_2)] \}. \end{aligned}$$

We will need the strain rates in each of the four corners of the grid cell. For the northeast corner, $(\xi_1, \xi_2) = (1, 1)$; for the southeast corner, $(\xi_1, \xi_2) = (1, 0)$, and so on. Thus, incorporating the above approximations into equation (15),

$$\begin{aligned} D_T^{ne} = \frac{1}{\bar{h}_1 \bar{h}_2} [\bar{h}_2 (u^{ne} - u^{nw}) - \Delta_1 h_2 u^{ne} - \bar{h}_1 (v^{ne} - v^{se}) \\ + \Delta_2 h_1 v^{ne}]. \end{aligned}$$

Discretizations for the other strain rates at each of the four cell corners are found in a similar manner. These are listed in appendix B.

b. Stress divergence

Consider each term in (13) in turn. As illustrated in section 2a, the contribution of the σ_1 term to F_1 is given by the coefficients of u at a given velocity node in the discretized form of the integral $1/2 \int \sigma_1 D_D dA$. We have, from (13) and (16),

$$\begin{aligned} \frac{1}{2} \int_0^1 \int_0^1 \sigma_1 \left(h_2 \frac{\partial u}{\partial \xi_1} + u \frac{\partial h_2}{\partial \xi_1} \right) d\xi_1 d\xi_2 \\ = \frac{1}{2} \int_0^1 \frac{\partial u}{\partial \xi_1} \left(\int_0^1 h_2 \sigma_1 d\xi_1 \right) d\xi_2 \\ + \frac{1}{2} \int_0^1 \frac{\partial h_2}{\partial \xi_1} \left(\int_0^1 u \sigma_1 d\xi_1 \right) d\xi_2. \end{aligned}$$

Substituting bilinear forms for u and σ_1 , the first term becomes

$$\begin{aligned} \frac{\bar{h}_2}{4} \left\{ u^{nw} \left[-\frac{1}{3} (\sigma_1^{ne} + \sigma_1^{nw}) - \frac{1}{6} (\sigma_1^{se} + \sigma_1^{sw}) \right] \right. \\ + u^{ne} \left[\frac{1}{3} (\sigma_1^{ne} + \sigma_1^{nw}) + \frac{1}{6} (\sigma_1^{se} + \sigma_1^{sw}) \right] \\ + u^{sw} \left[-\frac{1}{3} (\sigma_1^{se} + \sigma_1^{sw}) - \frac{1}{6} (\sigma_1^{ne} + \sigma_1^{nw}) \right] \\ \left. + u^{se} \left[\frac{1}{3} (\sigma_1^{se} + \sigma_1^{sw}) + \frac{1}{6} (\sigma_1^{ne} + \sigma_1^{nw}) \right] \right\}. \end{aligned}$$

The second (metric) term becomes

$$\begin{aligned} \frac{\Delta_1 h_2}{2} \left\{ u^{nw} \left[\frac{1}{9} \sigma_1^{nw} + \frac{1}{18} (\sigma_1^{sw} + \sigma_1^{ne}) + \frac{1}{36} \sigma_1^{se} \right] \right. \\ + u^{ne} \left[\frac{1}{9} \sigma_1^{ne} + \frac{1}{18} (\sigma_1^{nw} + \sigma_1^{se}) + \frac{1}{36} \sigma_1^{sw} \right] \\ + u^{sw} \left[\frac{1}{9} \sigma_1^{sw} + \frac{1}{18} (\sigma_1^{nw} + \sigma_1^{se}) + \frac{1}{36} \sigma_1^{ne} \right] \\ \left. + u^{se} \left[\frac{1}{9} \sigma_1^{sw} + \frac{1}{18} (\sigma_1^{ne} + \sigma_1^{nw}) + \frac{1}{36} \sigma_1^{ne} \right] \right\}. \end{aligned}$$

The sum of the first and second terms, divided by the cell area, gives the contribution from σ_1 to the stress term in the momentum equation for u over the cell (i, j) . Since the velocity for cell (i, j) is located in the northeast corner, the total contribution to the u momentum at this corner consists of the contributions (summed) from the northeast corner of cell (i, j) , the southeast corner of cell $(i, j + 1)$, the northwest corner of cell $(i + 1, j)$, and the southwest corner of cell $(i + 1, j + 1)$. We change sign as indicated in (23) and list the complete discretization in appendix C.

As noted in section 2b, the boundary terms associated with integrating over each cell area in (23) are accounted for in this discretization. In the interior of the domain (that is, away from the mesh edges), the boundary terms cancel with those of neighboring grid cells. We employ an extra set of “ghost cells” surrounding the physical domain to enforce periodic boundary conditions along the ξ_2 axis; the northern and southern boundaries both lie in land masses. On land boundaries the ice velocity is zero and therefore the boundary terms are zero.

4. Simulation results

We begin by running the full Los Alamos sea ice model (CICE) with the Cartesian and curvilinear EVP discretizations for 14 yr each, from specified fields for the ice thickness and concentration: the ice area fraction is near unity throughout the Arctic, decreasing to zero at the climatological ice edge, and the area-weighted-average ice thickness is near 2 m. We use a parameterization for the ice strength P following Rothrock (1975), detailed in appendix D. CICE includes the energy-conserving ice thermodynamics model of Bitz and Lipscomb (1999) with four ice layers and one layer of snow, the linear remapping ice thickness distribution scheme of Lipscomb (2001), an ice ridging scheme following Flato and Hibler (1995) and Thorndike et al. (1975), and the second-order, multidimensional, positive definite advection transport algorithm (MPDATA) of Smolarkiewicz (1984). CICE also includes a thermodynamics-only, slab mixed layer model for the upper ocean whose sea surface temperature (SST) evolves depending on atmospheric fluxes passing through open

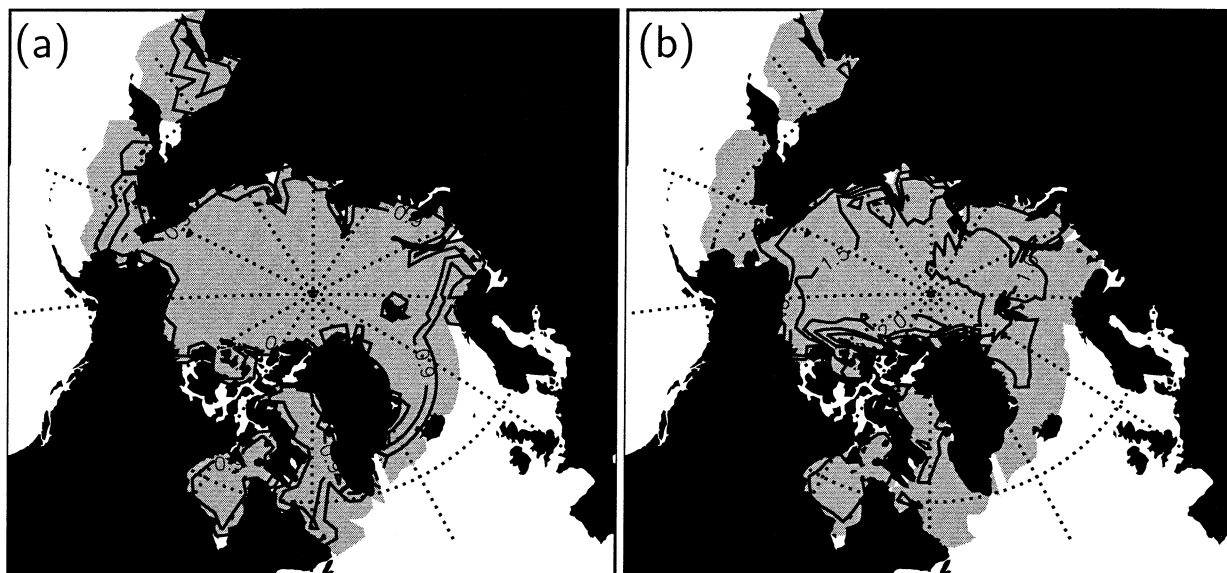


FIG. 2. (a) Ice concentration and (b) ice thickness on 1 Jan, after a 14-yr CICE integration using the curvilinear EVP discretization. Contour intervals are (a) [0.1, 0.9] and (b) 0.5 m. Regions with positive values are shaded.

water and leads in the ice cover, solar penetration through the ice, and heat fluxes associated with melting and freezing of ice (Hunke and Ackley 2001). Additional information about the CICE model is given in Hunke and Lipscomb (2001).

Wind stress is computed using bulk formulas with stability and quadratic dependence on the wind speed, following Bryan et al. (1996), with an ice surface roughness length of 5×10^{-4} m. Ocean stress is computed as in Hibler (1979) and Hunke and Dukowicz (1997), but only includes a contribution from the ice

motion, since the ocean currents are set to zero. The Coriolis parameter is latitude (ϕ) dependent, $f = 2(7.292 \times 10^{-5} \text{ s}^{-1}) \sin \phi$, and we integrate the model on the global displaced pole grids shown in Fig. 1. The EVP model parameters are defined as in Hunke (2001); $E = \zeta/T$, where $T = 1296\text{ s}$ is the damping timescale for elastic waves, and the EVP dynamics model is sub-cycled with a time step of 30 s under the forcing time step of 1 hr.

The model was run using a climatological dataset formed from 4 yr (1985–88) of bulk forcing data pro-

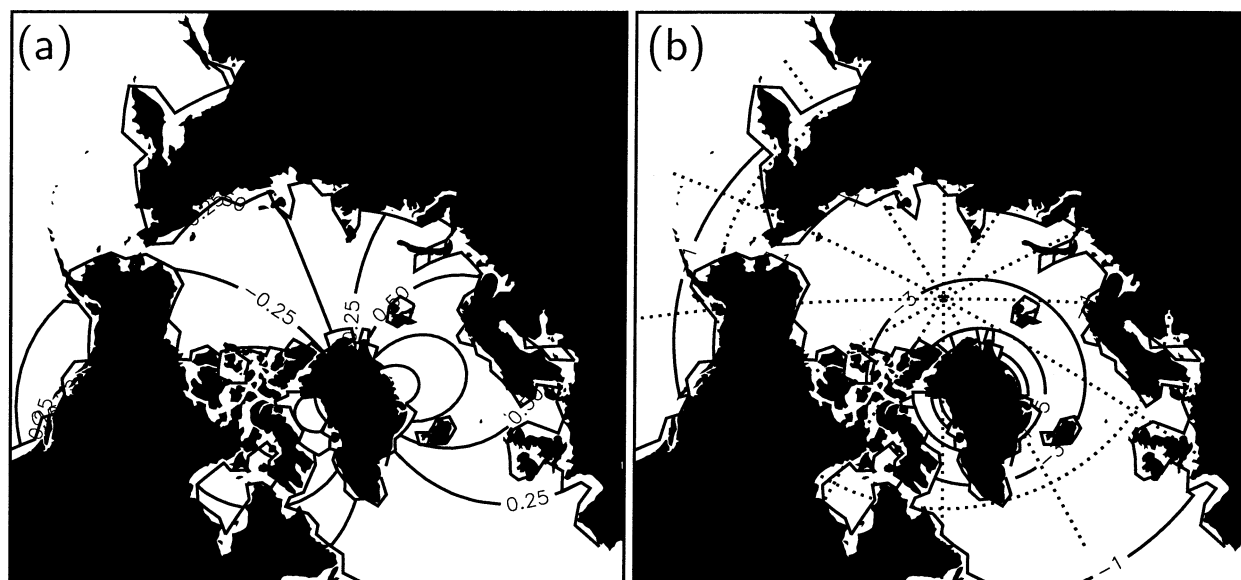


FIG. 3. Metric term coefficients (a) $\Delta_1 h_2 / \bar{h}_1 \bar{h}_2$, (b) $\Delta_2 h_1 / \bar{h}_1 \bar{h}_2$ (10^{-7} m^{-1}). Contour intervals are (a) $0.25 \times 10^{-7} \text{ m}^{-1}$ and (b) $2 \times 10^{-7} \text{ m}^{-1}$; contour lines along the coasts outline the land mask used in the simulations. A lat-lon grid is included in (b) for reference.

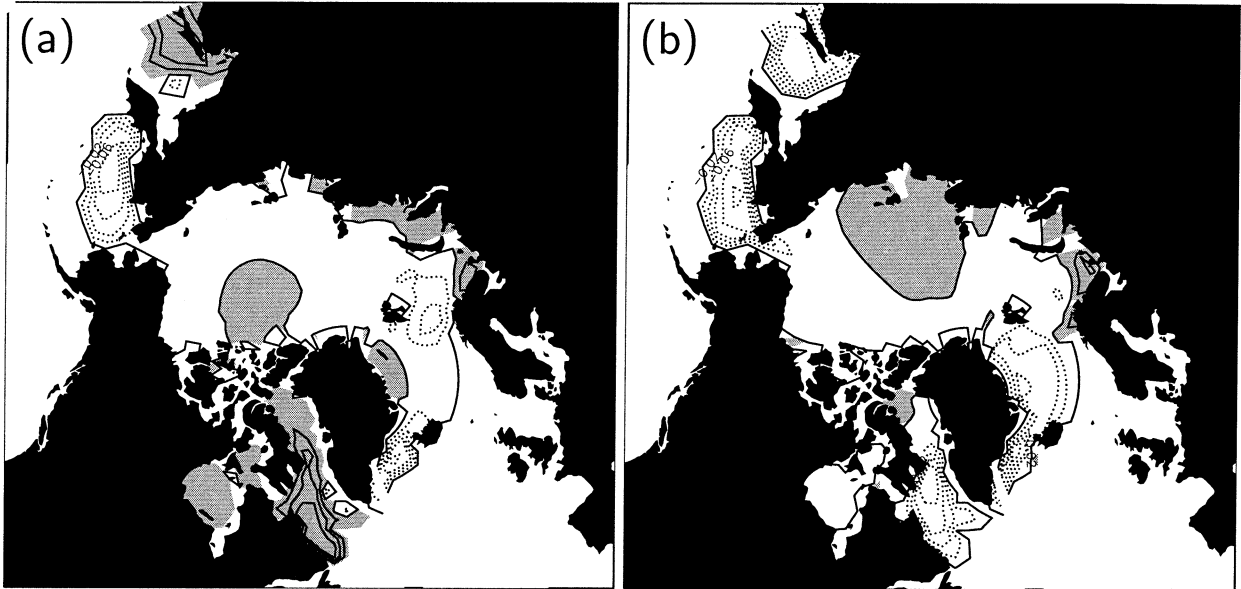


FIG. 4. Here, (a) u and (b) v velocity components averaged Jan–Mar, for the curvilinear simulation. Contour intervals are 0.02 m s^{-1} ; regions with positive values are shaded and negative contours are dotted.

vided by the National Center for Atmospheric Research, interpolated to the displaced pole grids. These data, described in Large et al. (1997), include 6-hourly, T62 resolution, 10-m data for air temperature, air density, specific humidity, and wind velocity from the National Centers for Environmental Prediction (NCEP) reanalyses, International Satellite Cloud Climatology Project (ISCCP) monthly downward shortwave radiation flux and cloud fraction, and blended monthly mean precipitation fields (Spencer 1993). The ocean freezing tem-

perature was determined from an annual mean salinity climatology (Levitus 1982), and a sea surface temperature climatology for January (Shea et al. 1990) was used to initialize the mixed layer model.

By the end of the 14-yr integrations, the annual cycle in the model simulations is in quasi equilibrium from one year to the next. We compare the ice state at the end of these two runs in section 4d, which highlights feedback effects when the ice strength varies in time. First, to clearly understand the effect

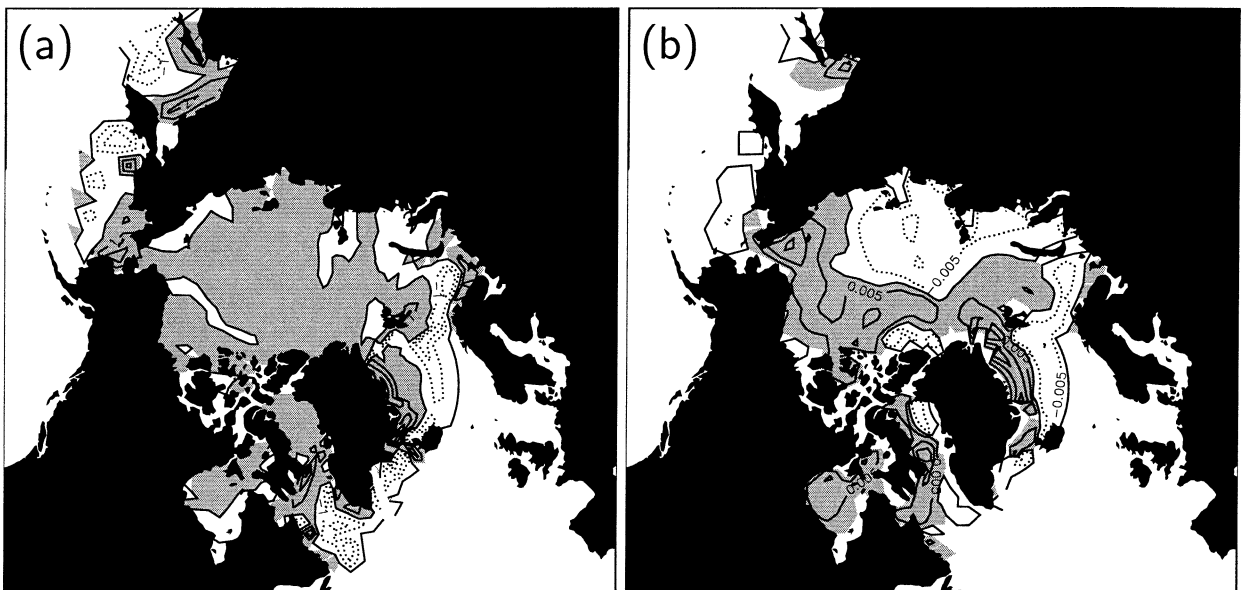


FIG. 5. Here, (a) $\nabla \cdot \mathbf{u}$ and (b) $(\nabla \cdot \sigma)_2$, averaged Jan–Mar, for the curvilinear simulation on the Gx3 mesh. Contour intervals are (a) $1\% \text{ day}^{-1}$ and (b) $-0.025, -0.015, -0.005, 0, 0.005, 0.015, 0.025 \text{ N m}^{-2}$. Regions with positive values are shaded and negative contours are dotted.

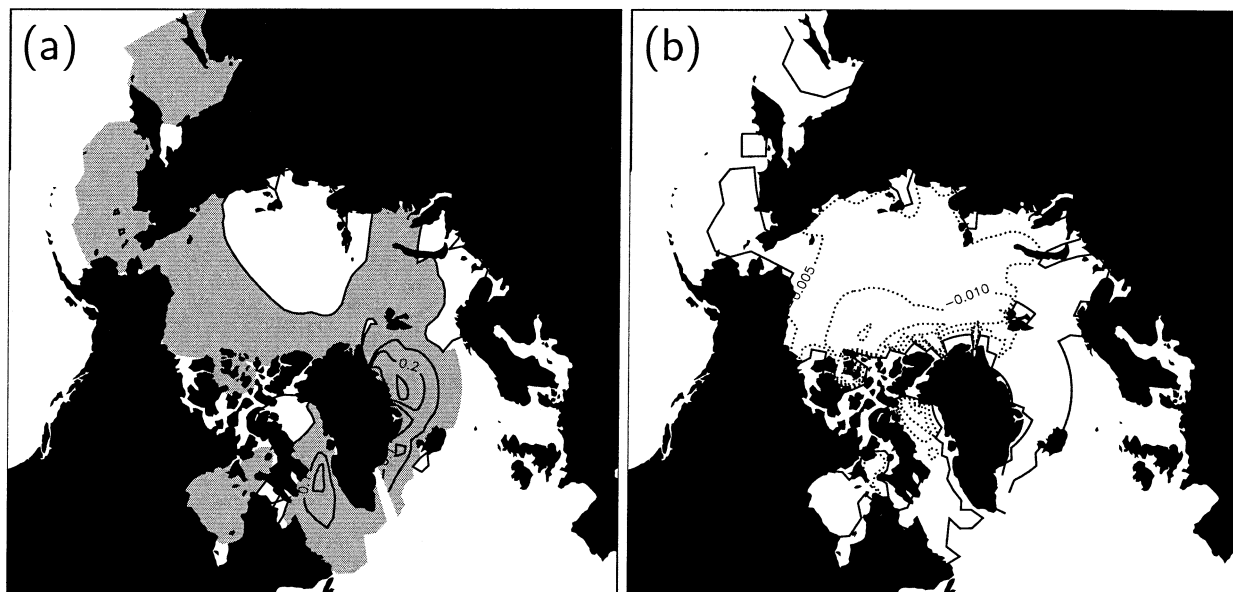


FIG. 6. Metric term contributions to (a) $\nabla \cdot \mathbf{u}$ and (b) $(\nabla \cdot \sigma)_2$ averaged Jan-Mar. Contour intervals are (a) $0.1\% \text{ day}^{-1}$ and (b) 0.005 N m^{-2} . Regions with positive values are shaded and negative contours are dotted.

of including the metric terms, we maintain ice strength P and mass m constant in time, so that feedbacks associated with time-varying ice thickness and concentration fields do not complicate the analysis. That is, we initialize P and m using the final ice concentration and thickness fields from the curvilinear spinup run, and then compare dynamics-only simulation results using the Cartesian and curvilinear discretizations on the coarse (Gx3) and fine (Gx1) meshes. The initial ice concentration and thickness fields

are illustrated in Fig. 2; initial ice velocity and internal stress are zero unless stated otherwise.

Although the dynamics-only simulations discussed later included both polar regions, we will focus attention on the Northern Hemisphere winter. As noted above, the metric terms are less important in the Southern Hemisphere because the Antarctic land mask extends outward from the southern pole farther than does Greenland in the north. We concentrate on the winter months because 1) without considering feedback effects, the ice internal stress is not

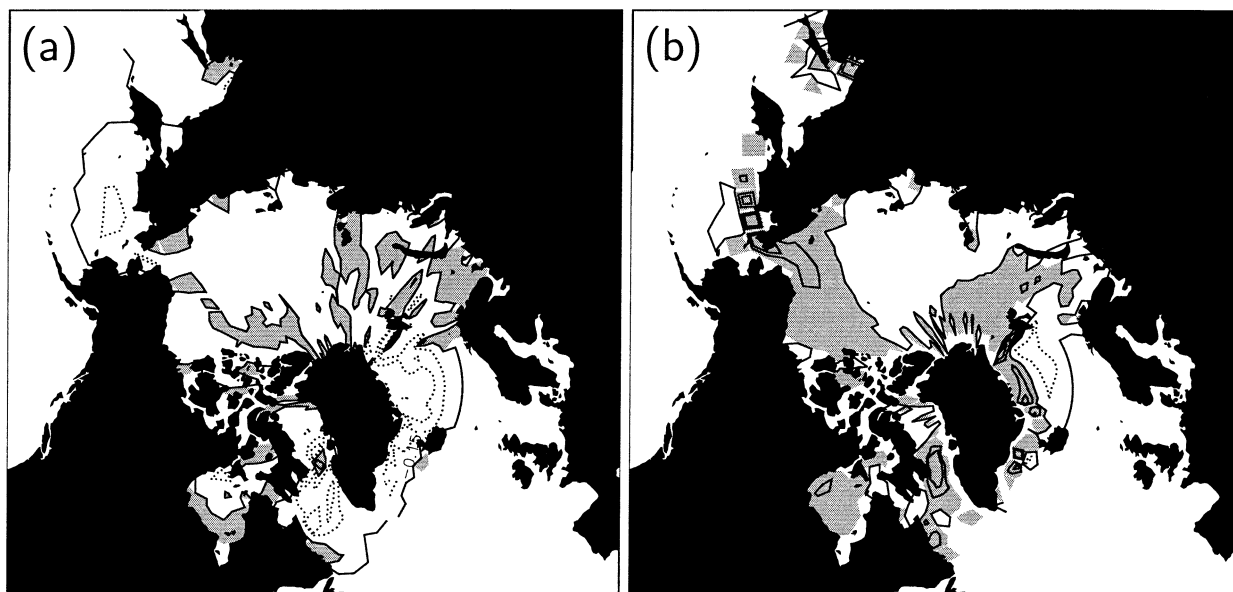


FIG. 7. Difference in (a) $\nabla \cdot \mathbf{u}$ and (b) $(\nabla \cdot \sigma)_2$ averaged Jan-Mar, between the two simulations (Cartesian-curvilinear). Contour intervals are (a) $0.15\% \text{ day}^{-1}$ and (b) 0.0015 N m^{-2} . Regions with positive values are shaded and negative contours are dotted.

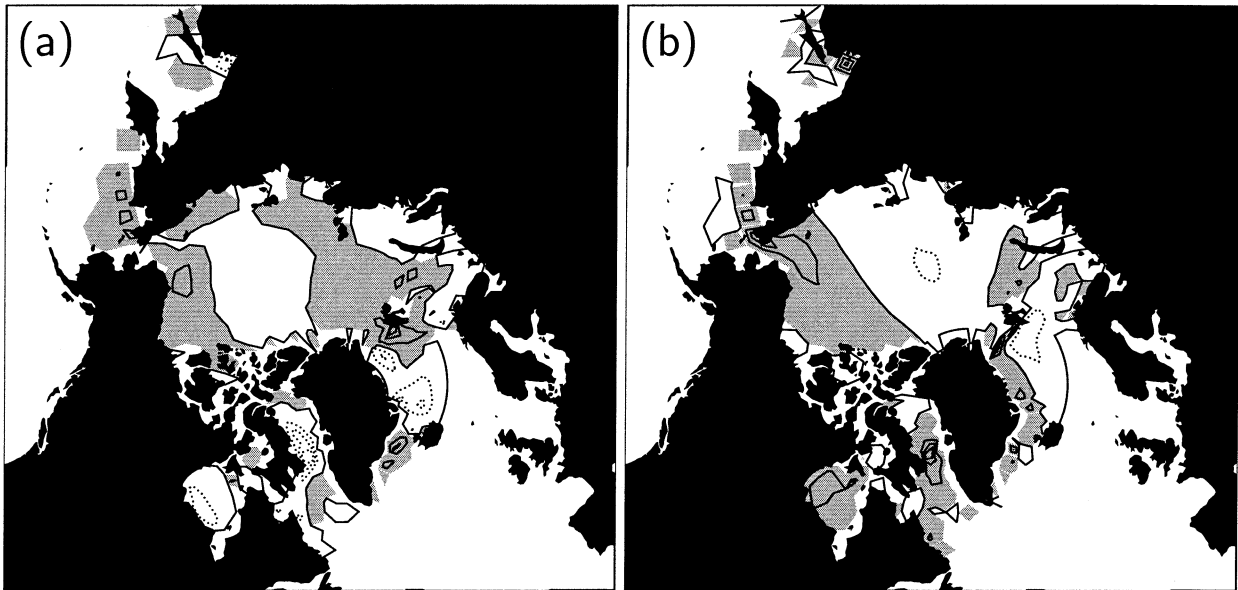


FIG. 8. Difference in (a) u and (b) v averaged Jan–Mar, between the two simulations (Cartesian–curvilinear). Contour intervals are 0.003 m s^{-1} ; regions with positive values are shaded and negative contours are dotted.

important in the summer months, when the ice is thinner and less compact; and 2) our nonevolving ice strength field is appropriate only for winter.

a. Coarse grid

Notice in Eqs. (17)–(19) that the metric terms are characterized by only two coefficients, namely,

$$\frac{1}{h_1 h_2} \frac{\partial h_1}{\partial \xi_2} \quad \text{and} \quad \frac{1}{h_1 h_2} \frac{\partial h_2}{\partial \xi_1}.$$

The numerical approximations, $\Delta_1 h_2 / \bar{h}_1 \bar{h}_2$ and $\Delta_2 h_1 / \bar{h}_1 \bar{h}_2$, are shown in Fig. 3. We associate the subscript “1” with lines of constant latitude in the Southern Hemisphere and the subscript “2” with lines of constant longitude, extending the association to the Northern

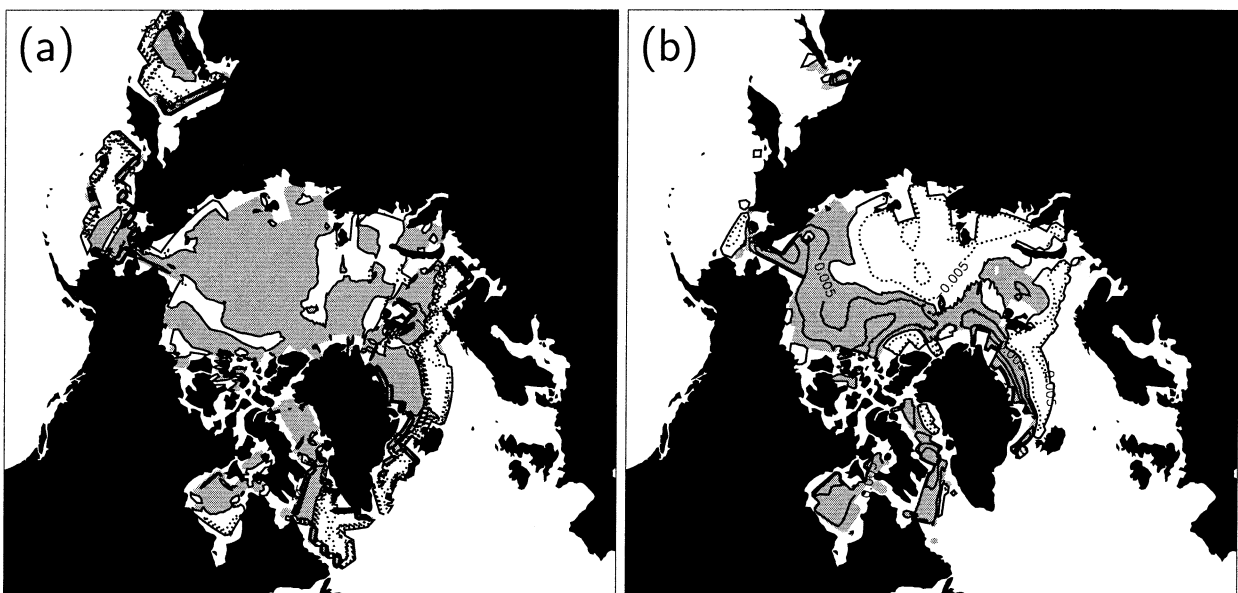


FIG. 9. Here, (a) $\nabla \cdot \mathbf{u}$ and (b) $(\nabla \cdot \sigma)_2$ averaged Jan–Mar, for the curvilinear simulation on the Gx1 mesh. Contour intervals are (a) $1\% \text{ day}^{-1}$ and (b) $-0.025, -0.015, -0.005, 0, 0.005, 0.015, 0.025 \text{ N m}^{-2}$. Regions with positive values are shaded and negative contours are dotted.

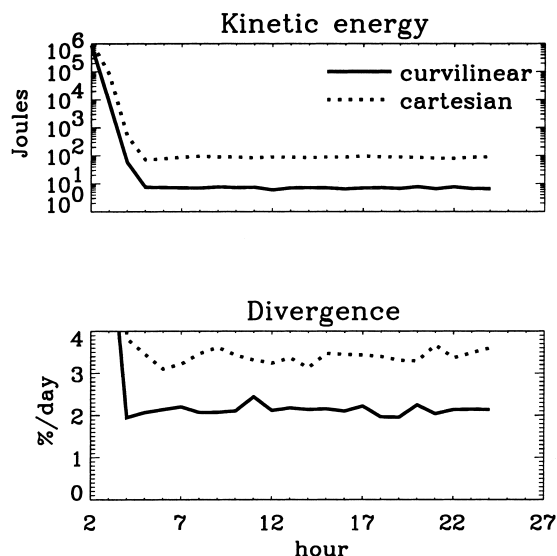


FIG. 10. Total global kinetic energy and divergence ($|D_D|$), summed over both polar regions. Only the “tail” is plotted for better resolution of the differences.

Hemisphere’s more general mesh. Due to the high curvature of the grid near Greenland, the coefficients approximating

$$\frac{1}{h_1 h_2} \frac{\partial h_1}{\partial \xi_2}$$

(Fig. 3b) are an order of magnitude larger than those approximating

$$\frac{1}{h_1 h_2} \frac{\partial h_2}{\partial \xi_1}$$

(Fig. 3a), and therefore we expect to see larger differences in variables associated with the ξ_2 (v) component of the momentum balance.

As a baseline for comparison purposes, the ice velocity components, divergence, and the ξ_2 component of internal stress divergence from the curvilinear simulation are shown in Figs. 4 and 5. Figure 6 shows the metric terms contributing to the ice divergence and ξ_2 component of internal stress divergence, hereafter notated $\nabla \cdot \mathbf{u}$ and $(\nabla \cdot \sigma)_2$, respectively. (These terms, which have coefficients given above and illustrated in Fig. 3, are computed as shown in appendices B and C.) While the $\nabla \cdot \mathbf{u}$ metric term is an order of magnitude smaller than $\nabla \cdot \mathbf{u}$ itself, the $(\nabla \cdot \sigma)_2$ metric term contributes significantly to $(\nabla \cdot \sigma)_2$.

The resulting change in the simulation is illustrated in Fig. 7, which shows the difference in $\nabla \cdot \mathbf{u}$ and $(\nabla \cdot \sigma)_2$ obtained by subtracting the curvilinear discretization results from the Cartesian discretization that did not include metric terms. Note that these differences also reflect changes in the basic discretization method, although we expect that including the metric terms explicitly has a greater effect than moving to bilinear approximations for the velocity and internal stress, since both discretizations are formally second-order accurate for uniform meshes. As expected, the change in $\nabla \cdot \mathbf{u}$ between the simulations is about an order of magnitude smaller than $\nabla \cdot \mathbf{u}$ itself, reflecting the presence of the metric terms. However, the change in $(\nabla \cdot \sigma)_2$ is much smaller than expected, given the relative magnitude of the metric term.

Scale analysis of the momentum balance provides an explanation for this result. Appropriate scales for the variables in the momentum equation are $m \sim 10^3$ kg

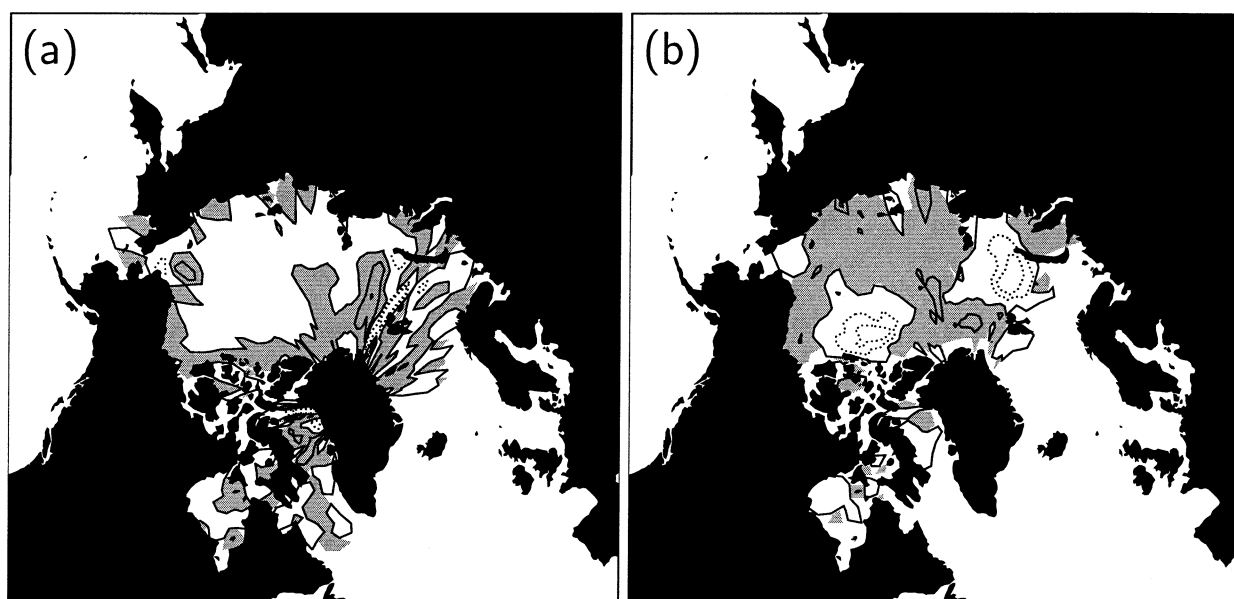


FIG. 11. Difference in (a) $\nabla \cdot \mathbf{u}$ and (b) $(\nabla \cdot \sigma)_2$ averaged Jul–Sep, between the two simulations (Cartesian–curvilinear) with time-varying ice strength and feedback effects. Contour intervals are (a) 0.15% day^{−1} and (b) 0.0005 N m^{−2}. Regions with positive values are shaded and negative contours are dotted.

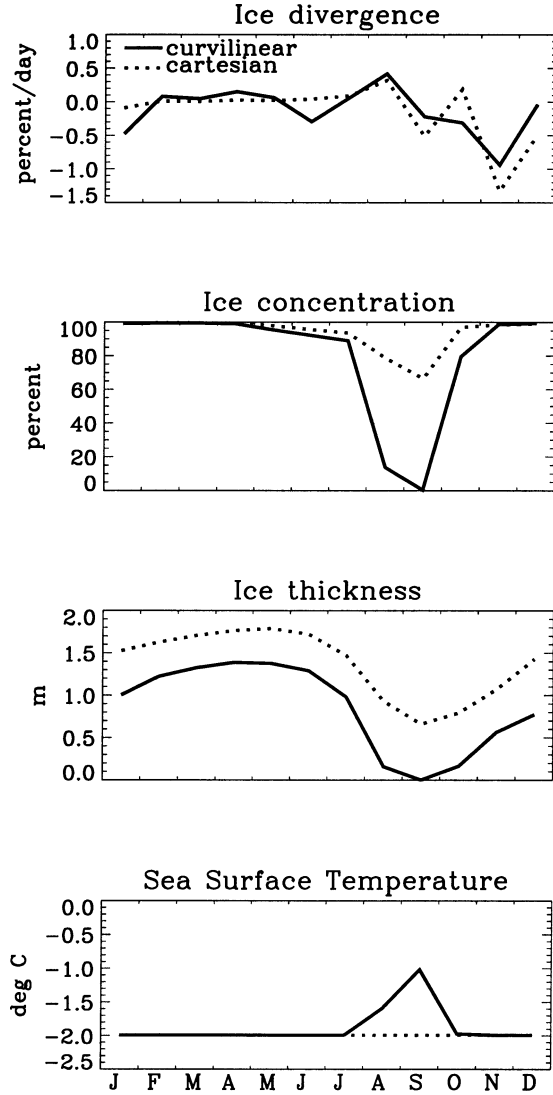


FIG. 12. Monthly averaged ice divergence, concentration, thickness, and sea surface temperature at the point (78.0°N, 54.2°E), for the curvilinear and Cartesian formulations.

m^{-2} , $f \sim 10^{-4} \text{ s}^{-1}$, $c_w \rho_w \sim 5 \text{ kg m}^{-3}$, $u \sim 10^{-2} \text{ m s}^{-1}$ and, for the seasonal timescale considered here, $\delta t \sim 10^7 \text{ s}$. With these values we have

$$\begin{aligned} \text{inertia:} & \quad \frac{mu}{\delta t} \sim 10^{-6} \text{ Nm}^{-2}, \\ \text{ocean stress:} & \quad c_w \rho_w u^2 \sim 5 \times 10^{-4} \text{ Nm}^{-2}, \\ \text{Coriolis:} & \quad mfu \sim 10^{-3} \text{ Nm}^{-2}, \\ \text{wind stress:} & \quad \tau_a \sim 10^{-2} \text{ Nm}^{-2}. \end{aligned}$$

As indicated in Fig. 5, the internal stress term is on the order of 10^{-2} N m^{-2} through the winter months. Therefore, because the other terms are all smaller by an order of magnitude or more, the wind stress and ice internal stress form the primary balance in the momentum equations for this timescale. Since the ice internal stress is effectively

constrained to cancel out the wind stress, irrespective of the metric terms, the metric terms make little difference. The difference in ice velocity between the runs is generally less than 0.003 m s^{-1} , shown in Fig. 8.

Thus, in spite of being relatively large, the metric terms may have only a small effect on sea ice simulation results, especially at the long timescales considered in climate studies. Without the feedback mechanisms associated with ice thermodynamics, advection, and ridging, however, we cannot draw such a conclusion with confidence. The ice divergence, D_D , may play a more prominent role when sophisticated ice distribution and ridging models (e.g., Thorndike et al. 1975) are incorporated (along with thermodynamics) into a full sea ice model. Similarly, the position of the ice edge, fixed in the previous simulation, may be more sensitive to differences in the stress divergence. A similar comparison of simulations with the full sea ice model, feedbacks included, is explored in section 4d.

b. Fine grid

The metric terms on the Gx1 grid shown in Fig. 1b are exactly the same as those on the Gx3 grid (Fig. 1a) because the Gx1 mesh is simply a more highly subdivided version of the Gx3 mesh. That is, the north and south poles reside in the same place on the sphere. Assuming that the grids are related by

$$h_1^{\text{Gx3}} = f_1 h_1^{\text{Gx1}}, \quad h_2^{\text{Gx3}} = f_2 h_2^{\text{Gx1}},$$

where $f_1, f_2 > 1$ are scaling factors between the grids, and since length is conserved,

$$dx = h_1 d\xi_1 = f_1 h_1 \frac{d\xi_1}{f_1}, \quad dy = h_2 d\xi_2 = f_2 h_2 \frac{d\xi_2}{f_2}.$$

we deduce that

$$f_1 \xi_1^{\text{Gx3}} = \xi_1^{\text{Gx1}}, \quad f_2 \xi_2^{\text{Gx3}} = \xi_2^{\text{Gx1}}.$$

Thus, for example,

$$\left[\frac{1}{h_1 h_2} \frac{\partial h_1}{\partial \xi_2} \right]^{\text{Gx3}} = \left[\frac{1}{(f_1 h_1)(f_2 h_2)} \frac{\partial (f_1 h_1)}{\partial \left(\frac{\xi_2}{f_2} \right)} \right]^{\text{Gx1}} = \left[\frac{1}{h_1 h_2} \frac{\partial h_1}{\partial \xi_2} \right]^{\text{Gx1}}.$$

As a result, metric terms do not play a strong role as resolution is changed. To the extent that spatial features are resolved in both calculations, the simulations should be similar. This is borne out by comparing Figs. 5 and 9. For these simulations, we interpolated the forcing data to the Gx1 mesh from the Gx3 mesh, rather than from the original, in order to filter higher spatial frequency modes and obtain a more direct comparison of discretization effects.

c. Dissipation

The total rate of internal work, D , provides another means of assessing the effect of the metric terms. Equations

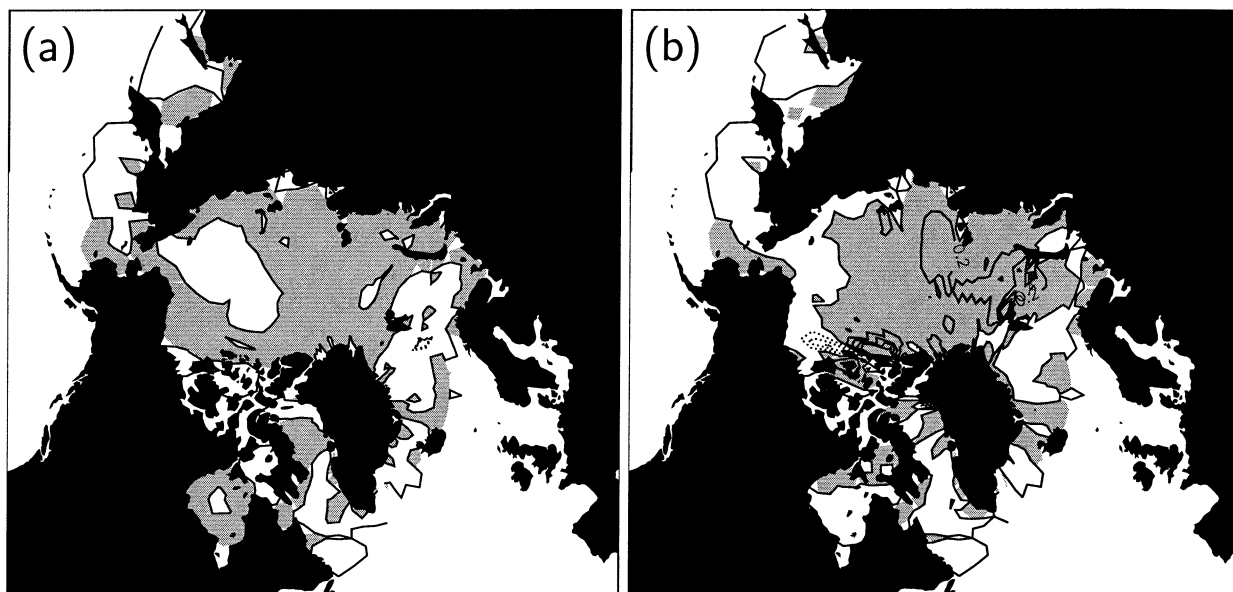


FIG. 13. Difference between the two simulations (Cartesian–curvilinear) in (a) ice concentration and (b) ice thickness on 1 Jan, after 14 yr of integration. Contour intervals are (a) 0.01 and (b) 0.2 m. Regions with positive values are shaded and negative contours are dotted.

tion (13) indicates that the dissipation rate depends on two factors, $\Delta - D_D$ and the ice strength P , with longer timescales when P is small. For this comparison we fix P and m with 90% concentration of 1-m-thick ice. With these initial ice conditions and an initial velocity field given by that at the end of the 14-yr curvilinear spinup, we run the model with the two discretization schemes under zero forcing conditions on the Gx3 grid, taking 24 1-h time steps.

Figure 10a illustrates the “spin-down” of total kinetic energy, $1/2 \sum m |\mathbf{u}|^2$ (summed over the entire globe), and Fig. 10b shows $\sum |D_D|$, where the divergence magnitude is used to avoid cancellations in the sum. The residual global kinetic energy is about 7 orders of magnitude smaller than the initial kinetic energy in the curvilinear case, and only 6 orders of magnitude smaller in the Cartesian case. At the same time, the curvilinear calculation has a more quiescent divergence field and correspondingly, a $1\% \text{ day}^{-1}$ lower residual total divergence than the Cartesian calculation. These results are related. As is evident from (13), dissipation is primarily associated with the D_S and D_T components of the strain rate, and not with divergence D_D . Since the curvilinear calculation has a lower level of residual divergence than the Cartesian case (Fig. 10b), it evidently had more shear and deformation, resulting in more dissipation and a lower level of kinetic energy, consistent with Fig. 10a. That is, the presence of metric terms in the curvilinear calculation [Eqs. (17)–(19)] raises the level of D_S and D_T in the strain rate, at the expense of D_D , resulting in more energy dissipation in this particular case.

d. Feedback effects

To assess the effects of changing ice thickness and concentration during the simulation, we compare the

final year of the spinup runs using the new curvilinear dynamics discretization and the older, Cartesian discretization. Because the distribution of ice does not change much over the first 3 months in either simulation, the differences in $\nabla \cdot \mathbf{u}$ and $(\nabla \cdot \sigma)_2$ are quite similar to those in Fig. 7 and are not shown. Larger differences occur later in the year, when melting and freezing rates may be affected by differing amounts of opening and closing within the ice pack.

In warmer months lower ice concentrations contribute to weak ice strength; internal stresses are small and the ice tends to drift freely. This is illustrated in Fig. 11, which shows averaged July–September values for $\nabla \cdot \mathbf{u}$ and $(\nabla \cdot \sigma)_2$. Although the internal stress forces are quite similar between the two runs (Fig. 11b), the ice divergence shown in Fig. 11a exhibits pronounced differences, $0.15\% \text{ day}^{-1}$ or more in the central Arctic. As the ice diverges, leads in the pack ice enlarge, allowing additional fluxes of radiation, heat, and moisture to pass between the atmosphere and ocean. Further heating of the mixed-layer can lead to additional ice melt in the summer, resulting in thinner ice and even more open water. This is evident in Fig. 12 for a point just west of Novaya Zemlya (78.0°N , 54.2°E). Thinner ice in the curvilinear simulation allows more ridging through ice convergence during June and subsequently a larger decrease in ice concentration than is evident in the Cartesian simulation. Enhanced by additional heating of the mixed layer, the increase in open water area accelerates until the ice thickness drops to zero, resulting in sea surface temperatures warmer in the curvilinear simulation by as much as 1°C . Although not accounted for in these

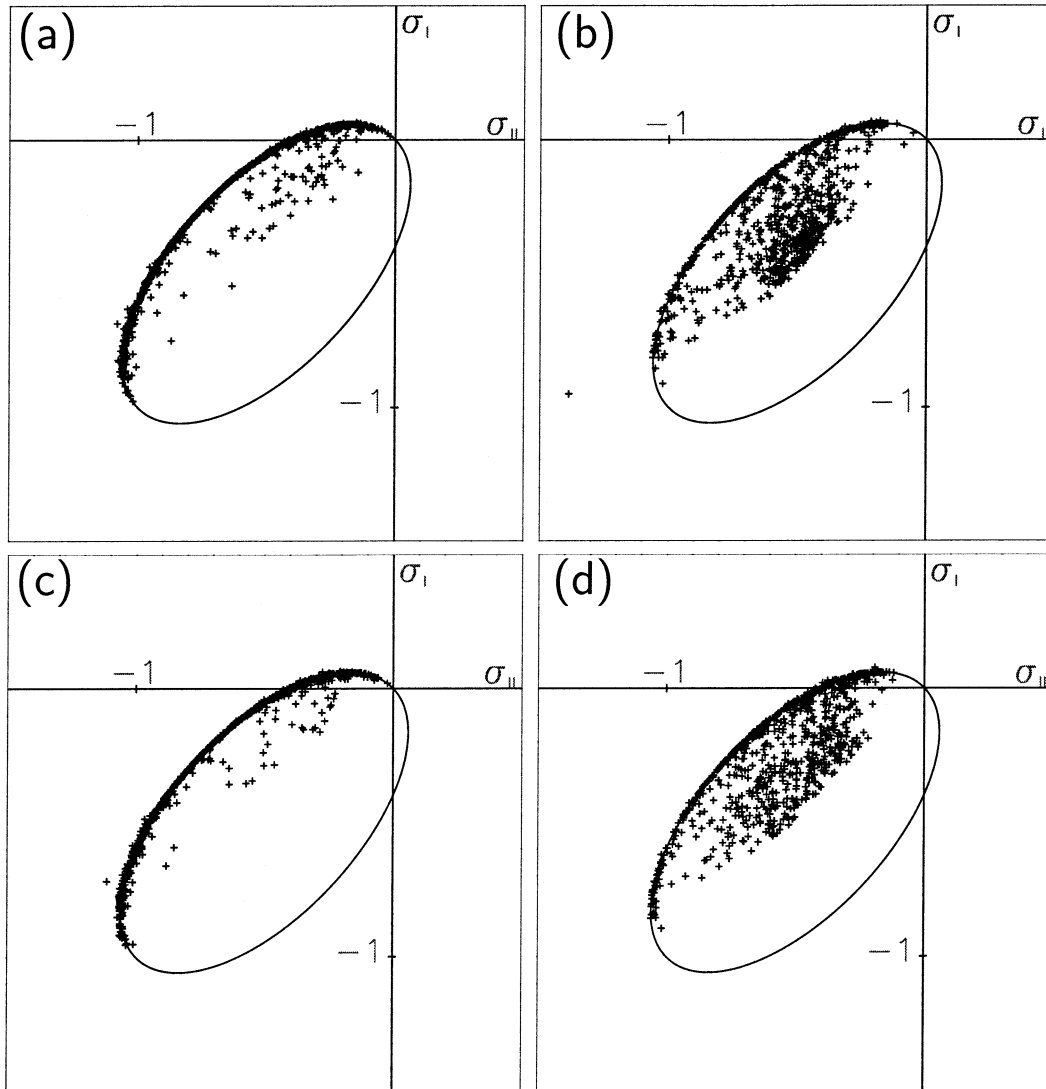


FIG. 14. Normalized principal stress states for the (a), (b) Cartesian and (c), (d) curvilinear spinup simulations on (a), (c) 1 Aug of the 14th integration year, and (b), (d) 1 Jan of year 15.

simulations, such a change in SST can affect atmospheric temperature and circulation significantly.

The example shown in Fig. 12 is an extreme case, however, and is not representative of differences over most of the Arctic Ocean. Although concentration differences may reach 20% or more near the ice edge or near coastlines, as in Fig. 12, ice concentrations typically differ by no more than a few percent in the central Arctic over the year, and by the end of December they are again quite close, near 100%, as shown in Fig. 13a. The ice thickness field represents a time-integrated measure of the differences between the two simulations, and is shown in Fig. 13b. While thickness differences are generally less than about 0.2 m over much of the Arctic basin, these simulations indicate that differences can be greater than 0.2 m over significant regional areas and reach several tens of cm near coasts.

e. Principal stress states

As a final note to this study, we demonstrate that the principal stress states produced with both discretizations obey the elliptical yield criterion (Fig. 14). Normalized by P , the principal stresses are given by

$$\sigma_I = \frac{1}{2P}(\sigma_1 + \sqrt{\sigma_2^2 + 4\sigma_{12}^2}),$$

$$\sigma_{II} = \frac{1}{2P}(\sigma_1 - \sqrt{\sigma_2^2 + 4\sigma_{12}^2}).$$

In summer (Figs. 14a,c), the ice is loosely packed, ice strength is low, and the ice is primarily in a state of plastic yielding. In winter (Figs. 14b,d), the ice is much more compact and in cells where the ice strength is large, the ice flows viscously, indicated by stresses lying inside the ellipse. Both discretizations capture this behavior, in con-

trast with the original EVP formulation (Hunke and Zhang 1999). For an extended discussion of principal stress states in the EVP model, see Hunke (2001).

5. Summary

In this paper we have demonstrated a variational method for deriving consistent operators for the ice dynamics that incorporate the metric terms while preserving the dissipative nature of the viscous–plastic ice rheology. In addition, within this approach we have discretized these operators using bilinear basis functions for the velocity and internal stress fields. This leads to a better behaved numerical discretization than in previous formulations, which approximated the velocity and internal stress components with linear and piecewise constant functions, respectively, over a grid cell.

Winter simulations with constant ice thickness and concentration indicate a remarkable insensitivity to the presence of metric terms. Although the internal stress metric terms may be large compared with the internal stress itself, the internal stress forces and therefore the ice motion are determined primarily by the wind stress, given the fixed ice strength; differences in the ice speed between the previous discretization and the present one are generally less than 0.005 m s^{-1} . Since grid variation is well resolved the metric terms are identical on a coarse grid as on a finer grid with the same mesh geometry, and the simulation results are therefore also the same.

However, grid curvature effects can be significant. In summer, when the ice floes are only loosely packed, the internal stress of the pack ice is near zero but divergence and convergence of the ice can be brisk. Deformation of the ice affects its thickness and concentration through ridging and thermodynamic growth and melt, which then alter the ice strength and its ability to deform further. Moreover, exposing a larger area of open water to the atmosphere allows increased flux exchange between the ocean and the atmosphere, ultimately resulting in less ice in summer, when the ocean warms due to solar heating, or more ice in winter, when sea surface cooling causes new ice to freeze. Under these conditions, including the metric terms results in generally thinner ice in the Arctic basin after 14 yr of integration. Therefore, we conclude that metric term effects are important when coupled with this deformation–strength feedback process, and these terms must be included for model discretizations on nonuniform grids.

Acknowledgments. This work has been supported by the DOE Climate Change Prediction Program. We extend thanks to Bill Lipscomb for his assistance with the thermodynamics and ridging model components used in this study, and to Bruce Briegleb for carefully reading and commenting on the manuscript.

APPENDIX A

Table of Symbols Used in the Text

Symbol	Definition	Units
ξ_i	i th spatial coordinate	
t	Temporal coordinate	s
h_i	Scale factor in the ξ_i direction	m
E	Elastic parameter	N m^{-1}
P	Ice pressure (strength)	N m^{-1}
m	Mass per unit area	kg m^{-2}
ζ	Bulk viscosity	kg s^{-1}
η	Shear viscosity	kg s^{-1}
e	Ratio of ellipse major and minor axes	2
Δ	Function of strain rates	s^{-1}
D	Rate of internal work	N m s^{-1}
D_D	Divergence, $\dot{\epsilon}_{11} + \dot{\epsilon}_{22}$	s^{-1}
D_S	Shearing strain rate, $2\dot{\epsilon}_{12}$	s^{-1}
D_T	Tension strain rate, $\dot{\epsilon}_{11} - \dot{\epsilon}_{22}$	s^{-1}
F_i	i th component of stress divergence	N m^{-2}
τ_i	i th component of surface stress	N m^{-2}
$\dot{\epsilon}_{ij}$	ij component of the strain rate tensor	s^{-1}
σ_{ij}	ij component of the stress tensor	N m^{-1}
σ_1	$\sigma_{11} + \sigma_{22}$	N m^{-1}
σ_2	$\sigma_{11} - \sigma_{22}$	N m^{-1}
$\mathbf{u} = (u, v)$	Ice velocity	m s^{-1}

APPENDIX B

Strain Rate Discretizations

a. Divergence

$$D_D^{\text{nc}} = \frac{1}{\bar{h}_1 \bar{h}_2} [\bar{h}_2 (u^{\text{nc}} - u^{\text{nw}}) + \Delta_1 h_2 u^{\text{nc}} + \bar{h}_1 (v^{\text{nc}} - v^{\text{se}}) + \Delta_2 h_1 v^{\text{nc}}]$$

$$D_D^{\text{nw}} = \frac{1}{\bar{h}_1 \bar{h}_2} [\bar{h}_2 (u^{\text{nc}} - u^{\text{nw}}) + \Delta_1 h_2 u^{\text{nw}} + \bar{h}_1 (v^{\text{nw}} - v^{\text{sw}}) + \Delta_2 h_1 v^{\text{nw}}]$$

$$D_D^{\text{se}} = \frac{1}{\bar{h}_1 \bar{h}_2} [\bar{h}_2 (u^{\text{se}} - u^{\text{sw}}) + \Delta_1 h_2 u^{\text{se}} + \bar{h}_1 (v^{\text{nc}} - v^{\text{se}}) + \Delta_2 h_1 v^{\text{se}}]$$

$$D_D^{\text{sw}} = \frac{1}{\bar{h}_1 \bar{h}_2} [\bar{h}_2 (u^{\text{se}} - u^{\text{sw}}) + \Delta_1 h_2 u^{\text{sw}} + \bar{h}_1 (v^{\text{nw}} - v^{\text{sw}}) + \Delta_2 h_1 v^{\text{sw}}]$$

b. Tension

$$D_T^{\text{ne}} = \frac{1}{\bar{h}_1 \bar{h}_2} [\bar{h}_2(u^{\text{ne}} - u^{\text{nw}}) - \Delta_1 h_2 u^{\text{ne}} - \bar{h}_1(v^{\text{ne}} - v^{\text{se}}) + \Delta_2 h_1 v^{\text{ne}}]$$

$$D_T^{\text{nw}} = \frac{1}{\bar{h}_1 \bar{h}_2} [\bar{h}_2(u^{\text{ne}} - u^{\text{nw}}) - \Delta_1 h_2 u^{\text{nw}} - \bar{h}_1(v^{\text{nw}} - v^{\text{sw}}) + \Delta_2 h_1 v^{\text{nw}}]$$

$$D_T^{\text{se}} = \frac{1}{\bar{h}_1 \bar{h}_2} [\bar{h}_2(u^{\text{se}} - u^{\text{sw}}) - \Delta_1 h_2 u^{\text{se}} - \bar{h}_1(v^{\text{ne}} - v^{\text{se}}) + \Delta_2 h_1 v^{\text{se}}]$$

$$D_T^{\text{sw}} = \frac{1}{\bar{h}_1 \bar{h}_2} [\bar{h}_2(u^{\text{se}} - u^{\text{sw}}) - \Delta_1 h_2 u^{\text{sw}} - \bar{h}_1(v^{\text{nw}} - v^{\text{sw}}) + \Delta_2 h_1 v^{\text{sw}}]$$

c. Shearing

$$D_S^{\text{ne}} = \frac{1}{\bar{h}_1 \bar{h}_2} [\bar{h}_1(u^{\text{ne}} - u^{\text{se}}) - \Delta_2 h_1 u^{\text{ne}} + \bar{h}_2(v^{\text{ne}} - v^{\text{nw}}) - \Delta_1 h_2 v^{\text{ne}}]$$

$$D_S^{\text{nw}} = \frac{1}{\bar{h}_1 \bar{h}_2} [\bar{h}_1(u^{\text{nw}} - u^{\text{sw}}) - \Delta_2 h_1 u^{\text{nw}} + \bar{h}_2(v^{\text{ne}} - v^{\text{nw}}) - \Delta_1 h_2 v^{\text{nw}}]$$

$$D_S^{\text{se}} = \frac{1}{\bar{h}_1 \bar{h}_2} [\bar{h}_1(u^{\text{ne}} - u^{\text{se}}) - \Delta_2 h_1 u^{\text{se}} + \bar{h}_2(v^{\text{se}} - v^{\text{sw}}) - \Delta_1 h_2 v^{\text{se}}]$$

$$D_S^{\text{sw}} = \frac{1}{\bar{h}_1 \bar{h}_2} [\bar{h}_1(u^{\text{nw}} - u^{\text{sw}}) - \Delta_2 h_1 u^{\text{sw}} + \bar{h}_2(v^{\text{se}} - v^{\text{sw}}) - \Delta_1 h_2 v^{\text{sw}}]$$

APPENDIX C

Discretizations for the Divergence of the Stress Tensor*a. Contribution of the σ_1 term to F_1*

$$\begin{aligned} \frac{1}{\bar{h}_1 \bar{h}_2} & \left\{ \left[-\frac{\bar{h}_2}{4} \left(\frac{1}{3} (\sigma_1^{\text{ne}} + \sigma_1^{\text{nw}}) + \frac{1}{6} (\sigma_1^{\text{se}} + \sigma_1^{\text{sw}}) \right) - \frac{\Delta_1 h_2}{2} \left(\frac{1}{9} \sigma_1^{\text{ne}} + \frac{1}{18} (\sigma_1^{\text{nw}} + \sigma_1^{\text{se}}) + \frac{1}{36} \sigma_1^{\text{sw}} \right) \right]_{ij} \right. \\ & + \left[\frac{\bar{h}_2}{4} \left(\frac{1}{3} (\sigma_1^{\text{ne}} + \sigma_1^{\text{nw}}) + \frac{1}{6} (\sigma_1^{\text{se}} + \sigma_1^{\text{sw}}) \right) - \frac{\Delta_1 h_2}{2} \left(\frac{1}{9} \sigma_1^{\text{nw}} + \frac{1}{18} (\sigma_1^{\text{sw}} + \sigma_1^{\text{ne}}) + \frac{1}{36} \sigma_1^{\text{se}} \right) \right]_{i+1j} \\ & + \left[-\frac{\bar{h}_2}{4} \left(\frac{1}{3} (\sigma_1^{\text{se}} + \sigma_1^{\text{sw}}) + \frac{1}{6} (\sigma_1^{\text{ne}} + \sigma_1^{\text{nw}}) \right) - \frac{\Delta_1 h_2}{2} \left(\frac{1}{9} \sigma_1^{\text{se}} + \frac{1}{18} (\sigma_1^{\text{ne}} + \sigma_1^{\text{sw}}) + \frac{1}{36} \sigma_1^{\text{nw}} \right) \right]_{ij+1} \\ & + \left. \left[\frac{\bar{h}_2}{4} \left(\frac{1}{3} (\sigma_1^{\text{se}} + \sigma_1^{\text{sw}}) + \frac{1}{6} (\sigma_1^{\text{ne}} + \sigma_1^{\text{nw}}) \right) - \frac{\Delta_1 h_2}{2} \left(\frac{1}{9} \sigma_1^{\text{sw}} + \frac{1}{18} (\sigma_1^{\text{nw}} + \sigma_1^{\text{se}}) + \frac{1}{36} \sigma_1^{\text{ne}} \right) \right]_{i+1j+1} \right\} \end{aligned}$$

b. Contribution of the σ_1 term to F_2

$$\begin{aligned} \frac{1}{\bar{h}_1 \bar{h}_2} & \left\{ \left[-\frac{\bar{h}_1}{4} \left(\frac{1}{3} (\sigma_1^{\text{ne}} + \sigma_1^{\text{se}}) + \frac{1}{6} (\sigma_1^{\text{nw}} + \sigma_1^{\text{sw}}) \right) - \frac{\Delta_2 h_1}{2} \left(\frac{1}{9} \sigma_1^{\text{ne}} + \frac{1}{18} (\sigma_1^{\text{nw}} + \sigma_1^{\text{se}}) + \frac{1}{36} \sigma_1^{\text{sw}} \right) \right]_{ij} \right. \\ & + \left[-\frac{\bar{h}_1}{4} \left(\frac{1}{3} (\sigma_1^{\text{nw}} + \sigma_1^{\text{sw}}) + \frac{1}{6} (\sigma_1^{\text{ne}} + \sigma_1^{\text{se}}) \right) - \frac{\Delta_2 h_1}{2} \left(\frac{1}{9} \sigma_1^{\text{nw}} + \frac{1}{18} (\sigma_1^{\text{sw}} + \sigma_1^{\text{ne}}) + \frac{1}{36} \sigma_1^{\text{se}} \right) \right]_{i+1j} \\ & + \left[\frac{\bar{h}_1}{4} \left(\frac{1}{3} (\sigma_1^{\text{ne}} + \sigma_1^{\text{se}}) + \frac{1}{6} (\sigma_1^{\text{nw}} + \sigma_1^{\text{sw}}) \right) - \frac{\Delta_2 h_1}{2} \left(\frac{1}{9} \sigma_1^{\text{sw}} + \frac{1}{18} (\sigma_1^{\text{ne}} + \sigma_1^{\text{sw}}) + \frac{1}{36} \sigma_1^{\text{nw}} \right) \right]_{ij+1} \\ & + \left. \left[\frac{\bar{h}_1}{4} \left(\frac{1}{3} (\sigma_1^{\text{nw}} + \sigma_1^{\text{sw}}) + \frac{1}{6} (\sigma_1^{\text{ne}} + \sigma_1^{\text{se}}) \right) - \frac{\Delta_2 h_1}{2} \left(\frac{1}{9} \sigma_1^{\text{sw}} + \frac{1}{18} (\sigma_1^{\text{nw}} + \sigma_1^{\text{se}}) + \frac{1}{36} \sigma_1^{\text{ne}} \right) \right]_{i+1j+1} \right\} \end{aligned}$$

APPENDIX D

Ice Strength Formulation

Following Rothrock (1975), we assume that the strength P is proportional to the change in ice potential energy per unit area of compressive deformation.

$$P = \frac{C_f g \rho_i (\rho_w - \rho_i)}{2 \rho_w} \left[r_o + \sum_{n=1}^N r_n (1 - k_n) \right]^{-1} \times \sum_{n=1}^N r_n \left[-h_n^2 + \frac{k_n}{3} \left(\frac{H_n^3 - H_{n-1}^3}{H_n - H_{n-1}} \right) \right], \quad (D1)$$

where

$$r_n = \begin{cases} \frac{2}{G^*} (G_n - G_{n-1}) \left(1 - \frac{G_{n-1} + G_n}{2G^*} \right) & \text{if } G_n < G^* \\ \frac{2}{G^*} (G^* - G_{n-1}) \left(1 - \frac{G_{n-1} + G^*}{2G^*} \right) & \text{if } G_{n-1} < G^* \leq G_n \\ 0 & \text{if } G^* \leq G_{n-1}. \end{cases}$$

Here, G_n is the fractional area covered by ice in categories 0 to n , and we take $G^* = 0.15$. Note that if the open water area is greater than G^* , then $G_{n-1} \geq G^*$ for all ice categories and we set $P = 0$.

REFERENCES

- Aris, R., 1962: *Vectors, Tensors, and the Basic Equations of Fluid Mechanics*. Prentice-Hall, 286 pp.
- Batchelor, G. K., 1967: *An Introduction to Fluid Dynamics*. Cambridge University Press, 615 pp.
- Bitz, C. M., and W. H. Lipscomb, 1999: An energy-conserving thermodynamic sea ice model for climate study. *J. Geophys. Res.*, **104C**, 15 669–15 677.
- Bryan, F. O., B. G. Kauffman, W. G. Large, and P. R. Gent, 1996: The NCAR CSM flux coupler. Tech. Note TN-425+STR, National Center for Atmospheric Research, 52 pp.
- Flato, G. M., and W. D. Hibler, 1992: Modeling pack ice as a cavitating fluid. *J. Phys. Oceanogr.*, **22**, 626–651.
- , and —, 1995: Ridging and strength in modeling the thickness distribution of Arctic sea ice. *J. Geophys. Res.*, **100C**, 18 611–18 626.
- Hibler, W. D., 1979: A dynamic thermodynamic sea ice model. *J. Phys. Oceanogr.*, **9**, 817–846.
- Hunke, E. C., 2001: Viscous-plastic sea ice dynamics with the EVP model: Linearization issues. *J. Comput. Phys.*, **170**, 18–38.
- , and J. K. Dukowicz, 1997: An elastic-viscous-plastic model for sea ice dynamics. *J. Phys. Oceanogr.*, **27**, 1849–1867.
- , and S. F. Ackley, 2001: A numerical investigation of the 1997–98 Ronne Polynya. *J. Geophys. Res.*, **106C**, 22 373–22 382.
- , and W. H. Lipscomb, 2001: CICE: The Los Alamos sea ice model, Documentation and software, version 3. Tech. Report LA-CC-98-16, Los Alamos National Laboratory, Los Alamos, NM, 52 pp. [Available online at <http://www.acl.lanl.gov/climate/>.]
- , and Y. Zhang, 1999: A comparison of sea ice dynamics models at high resolution. *Mon. Wea. Rev.*, **127**, 396–408.
- Large, W. G., G. Danabasoglu, S. C. Doney, and J. C. McWilliams, 1997: Sensitivity to surface forcing and boundary layer mixing in a global ocean model: Annual-mean climatology. *J. Phys. Oceanogr.*, **27**, 2418–2447.
- Levitus, S., 1982: *Climatological Atlas of the World Ocean*. NOAA Prof. Paper 13, U.S. Dept. of Commerce, 173 pp. and 17 microfiche.
- Lipscomb, W. H., 2001: Remapping the thickness distribution in sea ice models. *J. Geophys. Res.*, **106C**, 13 989–14 000.
- Rothrock, D. A., 1975: The energetics of the plastic deformation of pack ice by ridging. *J. Geophys. Res.*, **80**, 4514–4519.
- Shea, D. J., K. E. Trenberth, and R. W. Reynolds, 1990: A global monthly sea surface temperature climatology. NCAR Tech. Note NCAR/TN-345, National Center for Atmospheric Research, 167 pp.
- Smith, R. D., S. Kortas, and B. Meltz, 1995: Curvilinear coordinates for global ocean models. Tech. Rep. LA-UR-95-1146, Los Alamos National Laboratory, 53 pp.
- Smolarkiewicz, P. K., 1984: A fully multidimensional positive definite advection transport algorithm with small implicit diffusion. *J. Comput. Phys.*, **54**, 325–362.
- Spencer, R. W., 1993: Global oceanic precipitation from the MSU during 1979–91 and comparisons to other climatologies. *J. Climate*, **6**, 1301–1326.
- Thorndike, A. S., D. A. Rothrock, G. A. Maykut, and R. Colony, 1975: The thickness distribution of sea ice. *J. Geophys. Res.*, **80**, 4501–4513.

$$k_n = \frac{2h_n}{H_{n-1} + H_n}.$$

The empirical parameter $C_f = 17$ accounts for frictional energy dissipation (Flato and Hibler 1995); $g = 9.806 \text{ m s}^{-2}$ is gravitational acceleration; $\rho_i = 917 \text{ kg m}^{-3}$ and $\rho_w = 1026 \text{ kg m}^{-3}$ are the densities of ice and sea water, respectively. The mean thickness of ice in category n is denoted h_n , and the maximum thickness for each of our $N = 5$ thickness categories is $H_n = 0.6445 \text{ m}$, 1.391 m , 2.470 m , 4.567 m , 9.334 m . The maximum thickness for category $n = 0$, equivalent to the minimum ice thickness, is 0 m . The ratio of ice area ridging in category n to the total area of ridging ice is given by